# Characterizing second-order Raman modes in monolayer $MoSe_2$

Renhui Liu,[1,2,*] Lin-Han Li,[3,4,*] Ye Zhang,[1,2] Jianqi Huang,[5,†] Miao-Ling Lin,[3,4] Nguyen Tuan Hung,[6] Huaihong Guo,[7,‡] Zhenhua Wang,[1,2] Zhidong Zhang,[1,2] Riichiro Saito,[8] Ping-Heng Tan,[3,4,§] and Teng Yang[1,2,‖]

[1]*School of Materials Science and Engineering, University of Science and Technology of China, Shenyang 110016, China*

[2]*Shenyang National Laboratory for Materials Science, Institute of Metal Research, Chinese Academy of Sciences, Shenyang 110016, China*

[3]*State Key Laboratory of Semiconductor Physics and Chip Technologies, Institute of Semiconductors, Chinese Academy of Sciences, Beijing 100083, China*

[4]*Center of Materials Science and Optoelectronics Engineering, University of Chinese Academy of Sciences, Beijing 100049, China*

[5]*Institute of Quantum Materials and Devices, Liaoning Academy of Materials, Shenyang 110167, China*

[6]*Frontier Research Institute for Interdisciplinary Sciences, Tohoku University, Sendai 980-8578, Japan*

[7]*College of Sciences, Liaoning Petrochemical University, Fushun 113001, China*

[8]*Department of Physics, Tohoku University, Sendai 980-8578, Japan*

(Received 13 May 2025; accepted 23 July 2025; published 12 August 2025)

Sixteen second-order Raman modes of monolayer $MoSe_2$ are observed and analyzed by experiment and calculation, respectively, for four laser energies from 2.33–2.60 eV. The Raman peaks labeled by $P_i$ ($i = 1, 2, 3, 4$) at 280–320 $cm^{-1}$ and $S_i$ ($i = 1, 2, 3$) at 400–480 $cm^{-1}$ are newly analyzed quantitatively by the first-principles calculation using QR$^2$-CODE. The $P_i$ bands are assigned to the second-order combination modes of TA (LA) and $E'_{TO}$ ($E'_{LO}$), while the $S_i$ bands are assigned to the 2LA mode with different phonon wave vectors, which is explained by the combination of two-phonon density of states and electron-phonon coupling calculations. The overlapped Raman peak of the first-order mode E′ and the second-order mode $S_1$ can be identified separately using helicity-dependent Raman spectroscopy. The mode assignments are further confirmed by space-group analysis and helicity-dependent selection rule.

DOI: 10.1103/vvkp-9sth

## I. INTRODUCTION

Raman spectroscopy is a versatile technique for the fast, noninvasive, and highly sensitive characterization of the structure and physical properties of two-dimensional (2D) materials [1–5]. In particular, second-order double resonance Raman (DRR) modes, which involve two non-zone-centered phonons with wave vectors of $\boldsymbol{q}$ and $-\boldsymbol{q}$ [6,7], are widely observed in transition-metal dichalcogenides (TMDs) [8–16]. In the case of 2D semiconductors, since the flat electronic energy bands lead to a large electronic density of states, the DRR peaks can be seen clearly compared with three-dimensional semiconductors. Thus, the analysis of two-phonon double resonance Raman spectra can be analyzed quantitatively for 2D materials. DRR spectroscopy serves as a sensitive probe for defects in monolayer $MoS_2$ [17,18], confirms monolayer thickness in $WS_2$ by 2LA [19], and detects the quality of $MoSe_2$ monolayer samples grown by chemical vapor deposition (CVD) [14]. Furthermore, intervalley phonon scattering critically governs valley depolarization in TMDs-based valleytronics [12,20], while the softening of second-order modes directly evidences the charge-density-wave (CDW) phase transition in $NbSe_2$ [21]. For monolayer $MoSe_2$, the Raman intensities of the DRR modes are comparable to or even higher than those of the first-order Raman modes [10,22], providing an ideal platform for studying DRR modes and their underlying physics. Quantitative assignment of DRR modes that is compared with the single resonance Raman (SRR) modes is fundamental for interpreting Raman spectral profiles, elucidating electronic transitions, phonon symmetries, and the electron-phonon coupling (EPC) behind the spectra.

However, precise assignment of DRR modes for monolayer $MoSe_2$ remains controversial in the literature [13–15]. The controversy is caused by the difficulty of assigning DRR mode because the symmetry of each phonon wave vector $\boldsymbol{q}$ in the Brillouin zone (BZ) can be different. Furthermore, TMDs exhibit a relatively narrow frequency range in phonon dispersion and a flat phonon band compared with other 2D materials such as graphene, further complicating DRR mode assignment. Resolving this assignment controversy is therefore crucial for advancing our understanding of the DRR process by evaluating quantitative contribution of possible two-phonon pairs, which motivates this work.

To achieve a precise assignment of DRR modes for TMDs, numerous valuable studies and theoretical frameworks have been proposed; however, a consensus on the assignment of DRR modes has not been reached. Soubelet *et al.* [13] and Bilgin *et al.* [14] assigned all non-first-order Raman bands of monolayer $MoSe_2$ to the $n$th ($n = 2, 3, 4$)-order modes of M point, solely relying on the frequency relationship of the phonon dispersion. In particular, the peaks above 400 $cm^{-1}$

*These authors contributed equally to this work.
†Contact author: jqhuang@lam.ln.cn
‡Contact author: hhguo@alum.imr.ac.cn
§Contact author: phtan@semi.ac.cn
‖Contact author: yanghaiteng@msn.com

 

were assigned to the third- or fourth-order modes. In contrast, Sotgiu *et al.* [15] proposed the second-order nature for the Raman bands at high wave number (550–620 $cm^{-1}$) in bulk $MoSe_2$ using the two-phonon density of states (2phDOS) [23]. However, they have a limitation for mode assignments from all possible two-phonon modes in the calculation of 2phDOS. Moreover, these two methods do not provide the Raman scattering amplitude, phonon symmetry, and selection rule. To address these limitations, Huang *et al.* [24,25] developed a theoretical framework and computational QR$^2$-CODE based on first-principles calculations for quantitatively assigning and analyzing DRR modes, which has been applied in various 2D materials including graphene [26], $MoTe_2$ [24], $MoS_2$ [27,28], MoSSe [29], $ReS_2$ [30], etc. Furthermore, combining with first-principles calculation and group-theory analysis, Liu *et al.* [16] established the helicity selection rule of DRR modes in monolayer $MoSe_2$ with optical phonon branches involved.

However, since the previous version of QR$^2$-CODE calculates SRR and DRR spectra separately without normalization of the intensities, we can not compare the SRR and DRR intensities at the same time. When first-order and second-order Raman modes juxtapose in frequency, especially in the low-frequency region with acoustic phonon branches involved, it becomes difficult to distinguish their individual contribution and to separate the corresponding selection rules. This situation has happened in $MoSe_2$. Here, we introduce a renormalized intensity for both first- and second-order spectra, allowing a simultaneous analysis of overlapped modes and direct reproduction of the experimental spectra that consist of SRR and DRR spectra.

In this paper, we adopt monolayer $MoSe_2$ for analyzing 16 DRR modes that are observed by four laser energies 2.33–2.60 eV, which are resonant with the C exciton at ∼2.50 eV [31]. Then, using the updated QR$^2$-CODE [24,25], we successfully reproduce experimental spectra, incorporating both first- and second-order modes. We provide quantitative phonon mode assignments for all observed Raman spectra by Raman intensity as a function of phonon wave vector $\boldsymbol{q}$ in the BZ. In particular, the $S_1$–$S_3$ bands at 280–320 $cm^{-1}$ are assigned to 2LA from different $\boldsymbol{q}$. The overlapped Raman peak at ∼290 $cm^{-1}$ is assigned as a superposition of first-order mode E′ and second-order mode $S_1$. Space-group theory analysis [32–34] and selection rule of helicity-dependent Raman spectra confirm the symmetry of the DRR modes.

## II. METHODS

### A. Experimental method

The monolayer $MoSe_2$ sample was mechanically exfoliated from bulk crystals onto polydimethylsiloxane (PDMS) substrates and subsequently dry transferred onto $SiO_2/Si$ substrates. Raman spectroscopy measurements were performed in a backscattering geometry using two micro-Raman systems: a Jobin-Yvon HR800 and a LabRAM HR Evolution (Horiba Scientific), both equipped with 2400 grooves/mm gratings and liquid-nitrogen-cooled charge-coupled device (CCD) detectors. For room temperature characterization, the spectra were acquired through a 100× objective (numerical aperture, NA = 0.90) under ambient conditions. Low-temperature measurements were conducted using a closed-cycle cryostat system (attoDRY800, Attocube Systems AG) with the sample cooled to 4 K. In this configuration, a high-NA objective (NA = 0.82) was employed to optimize signal collection efficiency at cryogenic temperatures. The excitation energies are $E_L = 2.33$ eV (532 nm) from a diode-pumped solid-state laser, 2.41 eV (514 nm), 2.54 eV (488 nm), and 2.60 eV (477 nm) from an $Ar^+$ laser. The resolutions of the Raman system of these excitation energies are 0.27, 0.33, 0.36, and 0.44 $cm^{-1}$ per charge-coupled device (CCD) pixel, respectively.

### B. Computational method

All the electronic band structures and the phonon dispersion of $MoSe_2$ were calculated with the local density approximation (LDA) using QUANTUM ESPRESSO package [35]. We used relativistic norm-conserving pseudopotentials derived from an atomic Dirac-like equation [36] and a 160 Ry kinetic energy cutoff to carry out the calculation. The interlayer interaction of monolayer $MoSe_2$ was eliminated by maintaining a thick vacuum layer of 25 Å in a unit cell. The atomic structure was fully relaxed until the atomic force was less than $10^{-5}$ Ry/Bohr. The $18 \times 18 \times 1$ $\boldsymbol{k}$ grid and $9 \times 9 \times 1$ $\boldsymbol{q}$ grid Monkhorst-Pack meshes were used to sample the BZ for the calculation of electronic band structures and the phonon dispersion, respectively. Electronic structure and phonon dispersion relation were also calculated using DS-PAW software integrated in the DEVICE STUDIO program [37].

Then, using Wannier interpolation schemes as implemented in the EPW code [38,39], the EPC matrix elements for each phonon mode were obtained on a fine grid of $54 \times 54 \times 1$ $\boldsymbol{k}$ mesh and $\boldsymbol{q}$ mesh in the BZ, which is dense enough to achieve converged results. Finally, the Raman spectra under the same polarization configurations as the experiment were calculated using QR$^2$-CODE [25]. As shown in Fig. S1 of Supplemental Material (SM) [40], convergence tests confirm that the number of $\boldsymbol{k}$ mesh $N_{\boldsymbol{k}} \geqslant 54 \times 54$ ensures converged results for both first-order modes (the number of $\boldsymbol{q}$ mesh $N_{\boldsymbol{q}} = 1$ at Γ point) and second-order modes ($N_{\boldsymbol{q}} = N_{\boldsymbol{k}}$).

To directly compare first-order SRR with second-order DRR bands, we incorporate SRR and DRR bands in a single Raman spectrum. The workflow of calculating Raman spectra incorporating both SRR and DRR modes is as follows.

(i) Since a SRR process includes electron-phonon ($e$) and hole-phonon ($h$) subprocesses, the SRR tensor $\overleftrightarrow{R}_{\mathrm{SRR}}$ for the $\mu$th phonon mode at laser excitation energy $E_L$ is obtained by a summation of $\overleftrightarrow{R}_{\mathrm{SRR};a}$ over all $a$ subprocesses:

$$\overleftrightarrow{R}_{\mathrm{SRR}}(\mu, E_L) = \sum_{a=e,h} \overleftrightarrow{R}_{\mathrm{SRR};a}(\mu, E_L). \tag{1}$$

Using the third-order, time-dependent perturbation theory, the subprocess SRR tensor $\overleftrightarrow{R}_{\mathrm{SRR};a}$ can be obtained. For example, the tensor for the $e$ subprocess is calculated as follows,

$$\overleftrightarrow{R}_{\mathrm{SRR};e}(\mu, E_L) = \sum_{\boldsymbol{k},i=f,n,n'} \frac{\mathcal{D}_{fn'}(\boldsymbol{k}) \cdot \mathcal{M}_{n'n,\mu}(\boldsymbol{k}, \boldsymbol{0}) \cdot \mathcal{D}^{\dagger}_{ni}(\boldsymbol{k})}{(E_{ni} - E_L - i\gamma)(E_{fn'} - E_L \pm \hbar\omega_\mu - i\gamma)}, \tag{2}$$

where $i$, $n$ ($n'$), and $f$ denote the initial, intermediate, and final electron state, respectively. $\hbar$ is the reduced Planck constant, and $\omega_\mu$ denotes the frequency corresponding to $\mu$th phonon mode. The energy $E_{ni}$ ($E_{fn'}$) represents the vertical transition energy from the state $|i\rangle$ ($|n'\rangle$) to the state $|n\rangle$ ($|f\rangle$). The electric dipole matrix element is given by $\mathcal{D}_{ni} \equiv \langle n|\mathcal{D}|i\rangle$, and $\mathcal{M}_{n'n,\mu}(\boldsymbol{k},\boldsymbol{q})$ is the electron-phonon matrix elements at the electron wave vector $\boldsymbol{k}$ and phonon wave vector $\boldsymbol{q}$. For a SRR process, only zero wave vector phonon ($\boldsymbol{q}=\boldsymbol{0}$) contributes. The energy denominator $\gamma$ denotes the broadening in energy due to the finite lifetime of the photo-excited electrons. Here we empirically adopt $\gamma = 0.1$ eV in both SRR and DRR spectrum calculations. The $\pm$ signs in Eqs. (2)–(8) correspond to absorption (Stokes process, $-$) and emission (anti-Stokes process, $+$) of a phonon.

For a fixed Raman shift $\omega_{\mathrm{RS}}$, the Raman intensity for $\mu$th phonon mode can be derived from Raman tensor combined with the Jones vector of incident ($\boldsymbol{P}_{\mathrm{i}}$) and scattered light ($\boldsymbol{P}_{\mathrm{s}}$). The total SRR intensity $I_{\mathrm{SRR}}$ is by summing over the phonon mode $\mu$ as follows,

$$I_{\mathrm{SRR}}(\omega_{\mathrm{RS}}) \propto \sum_{\mu} |\boldsymbol{P}_{\mathrm{s}}^{\dagger} \cdot \overleftrightarrow{R}_{\mathrm{SRR}} \cdot \boldsymbol{P}_{\mathrm{i}}|^2 L(\hbar\omega_{\mathrm{RS}} \pm \hbar\omega_\mu) \equiv \sum_{\mu} I_{\mathrm{SRR}}^{\mu}, \tag{3}$$

where $L$ is a Lorentzian function to simulate energy-conservation $\delta$ function in Raman spectra as follows

$$L(\hbar\omega_{\mathrm{RS}} \pm \hbar\omega_\mu) = \frac{1}{\pi} \frac{\Gamma}{(\hbar\omega_{\mathrm{RS}} \pm \hbar\omega_\mu)^2 + \Gamma^2}, \tag{4}$$

where the broadening parameter $\Gamma$ comes from phonon lifetime. Here, we adopt the same value of $\Gamma = 6\,\mathrm{cm}^{-1}$ for each mode in our SRR spectrum calculation for simplicity.

(ii) Since a DRR process includes *ee*, *eh*, *he*, and *hh* four subprocesses, the $\boldsymbol{q}$-resolved DRR tensor $\overleftrightarrow{R}_{\mathrm{DRR}}$ for a combination of the $\mu$th and the $\nu$th phonon modes at $E_{\mathrm{L}}$ is calculated by summation of $\overleftrightarrow{R}_{\mathrm{DRR};a,b}$ over all $ab$ subprocesses:

$$\overleftrightarrow{R}_{\mathrm{DRR}}(\boldsymbol{q},\mu,\nu,E_{\mathrm{L}}) = \sum_{a,b=e,h} \overleftrightarrow{R}_{\mathrm{DRR};a,b}(\boldsymbol{q},\mu,\nu,E_{\mathrm{L}}). \tag{5}$$

Using the fourth-order, time-dependent perturbation theory [3], the $\boldsymbol{q}$-resolved DRR tensor $\overleftrightarrow{R}_{\mathrm{DRR};a,b}$ for an $ab$ subprocess can be obtained. Here $\overleftrightarrow{R}_{\mathrm{DRR};e,e}$ for the *ee* subprocess is given as follows as an example,

$$\overleftrightarrow{R}_{\mathrm{DRR};e,e}(\boldsymbol{q},\mu,\nu,E_{\mathrm{L}}) = \sum_{\boldsymbol{k},i=f,n,n',n''} \frac{\mathcal{D}_{fn''}(\boldsymbol{k}) \cdot \mathcal{M}_{n''n',\nu}(\boldsymbol{k}+\boldsymbol{q},-\boldsymbol{q}) \cdot \mathcal{M}_{n'n,\mu}(\boldsymbol{k},\boldsymbol{q}) \cdot \mathcal{D}_{ni}^{\dagger}(\boldsymbol{k})}{(E_{ni} - E_{\mathrm{L}} - \mathrm{i}\gamma)(E_{n'i} - E_{\mathrm{L}} \pm \hbar\omega_\mu - \mathrm{i}\gamma)(E_{fn''} - E_{\mathrm{L}} \pm \hbar\omega_\mu \pm \hbar\omega_\nu - \mathrm{i}\gamma)}. \tag{6}$$

Notations are consistent with those used in the SRR spectrum calculation. For a fixed Raman shift $\omega_{\mathrm{RS}}$, the total DRR intensity $I_{\mathrm{DRR}}$ is by summing over the phonon vectors $\boldsymbol{q}$ and $-\boldsymbol{q}$ in the Brillouin zone for $\mu$th and $\nu$th phonon modes as follows,

$$\begin{aligned} I_{\mathrm{DRR}}(\omega_{\mathrm{RS}}) &\propto \sum_{\boldsymbol{q},\mu,\nu} |\boldsymbol{P}_{\mathrm{s}}^{\dagger} \cdot \overleftrightarrow{R}_{\mathrm{DRR}} \cdot \boldsymbol{P}_{\mathrm{i}}|^2 L(\hbar\omega_{\mathrm{RS}} \pm \hbar\omega_\mu \pm \hbar\omega_\nu) \\ &\equiv \sum_{\boldsymbol{q},\mu,\nu} I_{\mathrm{DRR}}^{\boldsymbol{q}\mu\nu}. \end{aligned} \tag{7}$$

The Lorentzian function $L$ in Eq. (7) is expressed as follows,

$$L(\hbar\omega_{\mathrm{RS}} \pm \hbar\omega_\mu \pm \hbar\omega_\nu) = \frac{1}{\pi} \frac{\Gamma}{(\hbar\omega_{\mathrm{RS}} \pm \hbar\omega_\mu \pm \hbar\omega_\nu)^2 + \Gamma^2}. \tag{8}$$

Since DRR mode has larger full width at half-maxima (FWHM) than that of SRR mode, we adopt a larger $\Gamma = 8\,\mathrm{cm}^{-1}$ for each $\boldsymbol{q}$ point and each mode in our DRR spectrum calculation for simplicity.

(iii) Combining Eq. (3) with Eq. (7), the SRR intensity and DRR intensity are incorporated in a single Raman spectrum by normalizing the number of $\boldsymbol{q}$ points and the square of the number of $\boldsymbol{k}$ points adopted in Wannier interpolation, which is expressed as follows,

$$I(\omega_{\mathrm{RS}}) = \frac{I_{\mathrm{SRR}}(\omega_{\mathrm{RS}})}{N_{\boldsymbol{k}}^2} + \frac{I_{\mathrm{DRR}}(\omega_{\mathrm{RS}})}{N_{\boldsymbol{k}}^2 N_{\boldsymbol{q}}}, \tag{9}$$

where $I(\omega_{\mathrm{RS}})$ denotes total Raman intensity, and $N_{\boldsymbol{k}}$ and $N_{\boldsymbol{q}}$ represent the number of $\boldsymbol{k}$ and $\boldsymbol{q}$ points, respectively. Here, $N_{\boldsymbol{q}} = 1$ for SRR modes, thereby omitted in the term of SRR process in Eq. (9).

For the calculation of helicity-conserved ($\sigma^+\sigma^+$) and helicity-changing ($\sigma^+\sigma^-$) geometries, $\boldsymbol{P}_{\mathrm{i}}$ and $\boldsymbol{P}_{\mathrm{s}}$ are expressed as follows,

$$\begin{aligned} \sigma^+\sigma^+ &: \boldsymbol{P}_{\mathrm{i}} = \boldsymbol{P}_{\mathrm{s}} = \frac{1}{\sqrt{2}} \begin{pmatrix} 1 \\ \mathrm{i} \\ 0 \end{pmatrix}, \\ \sigma^+\sigma^- &: \boldsymbol{P}_{\mathrm{i}} = \frac{1}{\sqrt{2}} \begin{pmatrix} 1 \\ \mathrm{i} \\ 0 \end{pmatrix}, \quad \boldsymbol{P}_{\mathrm{s}} = \frac{1}{\sqrt{2}} \begin{pmatrix} 1 \\ -\mathrm{i} \\ 0 \end{pmatrix}. \end{aligned} \tag{10}$$

For the unpolarized geometry, the Raman intensity $I_{\mathrm{un}}$ is derived by the average value of the intensities in the $xx$ ($I_{xx}$), $xy$ ($I_{xy}$), $yx$ ($I_{yx}$), and $yy$ ($I_{yy}$) linearly polarized geometries as follows,

$$I_{\mathrm{un}} = \frac{I_{xx} + I_{xy} + I_{yx} + I_{yy}}{4}. \tag{11}$$

## III. RESULTS AND DISCUSSION

### A. Assignment of DRR modes

In Fig. 1(a), we show the Raman spectra of monolayer $MoSe_2$ in the unpolarized geometry at laser energy $E_{\mathrm{L}} = 2.33$ eV, where the calculated Raman spectra (bottom) can reproduce the experimental one (top) well. The Raman spectra of $E_{\mathrm{L}} = 2.41$, 2.54, and 2.60 eV are shown in Fig. S2 of SM [40]. Sixteen second-order

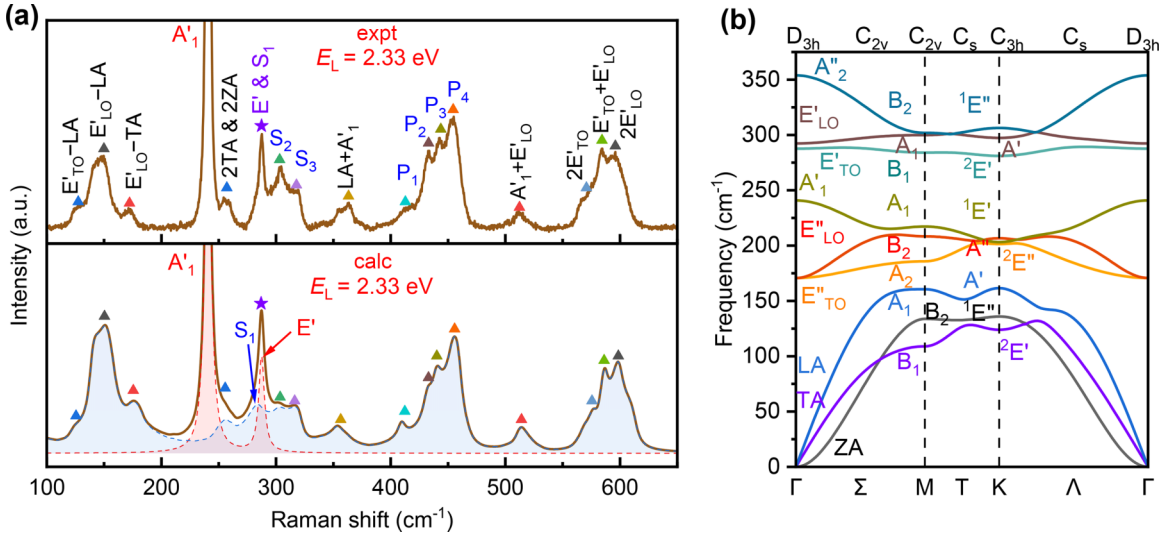


FIG. 1. (a) Raman spectra of monolayer $MoSe_2$ at laser energy $E_L = 2.33$ eV: experiment (top) and calculation (bottom). Si peak is subtracted in the experimental Raman spectra. Triangle and star denote second-order mode and superposition of first-order mode E′ and second-order mode $S_1$ (labeled E′ & $S_1$), respectively. The red and blue filled areas in the bottom panel represent calculated first- and second-order Raman spectra, respectively. (b) Calculated phonon dispersion for monolayer $MoSe_2$. The wave vector groups are listed above for each $\boldsymbol{q}$ point with the irreducible representations (Irreps) given on each band.

Raman modes are observed in both experimental and calculated Raman spectra. The peak position and peak shape agree reasonably well with those of the experiment. All assignments remain consistent for the four $E_L$. A detailed assignment of each DRR mode is listed in Table I and compared with the previous assignments by Soubelet *et al.* [13] and Bilgin *et al.* [14]. For convenience, we adopt the irreducible representation (Irrep) at the Γ point to represent the phonon branch, which is labeled in the phonon dispersion in Fig. 1(b).

For most bands below 400 cm$^{-1}$, our mode assignments generally align with the literature while revealing distinct differences in phonon contributions. In particular, three DRR bands $S_i$ ($i = 1, 2, 3$) at 280–320 cm$^{-1}$ are newly assigned to 2LA from different $\boldsymbol{q}$. Furthermore, the Raman bands observed at 110–190 cm$^{-1}$ are assigned to second-order combination modes involving coupled Stokes and anti-Stokes scattering processes, which is validated by the experimental temperature-dependent Raman spectra in Fig. S3 of SM [40]. But for the higher peaks above 400 cm$^{-1}$, we assign them only to second-order modes rather than higher-order modes, which is consistent with the second-order nature proposed by Sotgiu *et al.* [15]. Since the three bands at 560–610 cm$^{-1}$ have already been analyzed in our previous paper [16], we will

TABLE I. Comparison of assignments for the second-order modes between this work and Refs. [13,14]. The peak positions are measured at $E_L = 2.33$ eV.

| Peak position (cm$^{-1}$) | | Assignments | | | |
|---|---|---|---|---|---|
| Experiment | Calculation | Ref. [13] | Ref. [14] | This work | Label |
| 127.50 | 125.40 | – | – | $E'_{TO}$ − LA (∼ K) | |
| 149.92 | 150.40 | LA (M) | LA (M) & E′ − LA (M) | $E'_{LO}$ − LA (∼ K & Σ) | |
| 172.23 | 175.55 | E″(Γ) | E″(Γ) | $E'_{LO}$ − TA (∼ K) | |
| 257.03 | 255.60 | – | 2ZA | 2TA (Λ) & 2ZA (∼K) | |
| 287.32 | 284.00 | – | – | 2LA (Λ) | $S_1$ |
| 303.12 | 303.50 | 2LA (M) | 2LA (M) | 2LA (Σ) | $S_2$ |
| 317.78 | 316.30 | – | – | 2LA (∼M) | $S_3$ |
| 363.17 | 356.40 | LA + $A'_1$ (M) | LA + $A'_1$ (M) | LA + $A'_1$ (Λ) | |
| 412.77 | 412.30 | TA + 2LA (M) | TA + 2LA (M) | TA + $E'_{TO}$ (∼ K) | $P_1$ |
| 433.10 | 433.00 | LA + E′ (M) | ZA + 2LA (M) | TA + $E'_{LO}$ (∼ K) | $P_2$ |
| 443.74 | 440.00 | – | – | LA + $E'_{TO}$ (∼ M) | $P_3$ |
| 454.48 | 455.80 | 3LA (M) | 3LA (M) | LA + $E'_{LO}$ (∼ M) | $P_4$ |
| 512.32 | 514.10 | $A'_1$ + 2LA (M) | – | $A'_1$ + $E'_{LO}$ (Σ) | |
| 570.74 | 575.60 | TA + 3LA (M) | TA + 3LA (M) | 2$E'_{TO}$ (∼ M & Λ) | |
| 584.22 | 586.20 | E′ + 2LA (M) | E′ + 2LA (M) | $E'_{TO}$ + $E'_{LO}$ (∼ K) | |
| 597.29 | 598.60 | 4LA (M) | 4LA (M) | 2$E'_{LO}$ (∼ M & Λ) | |

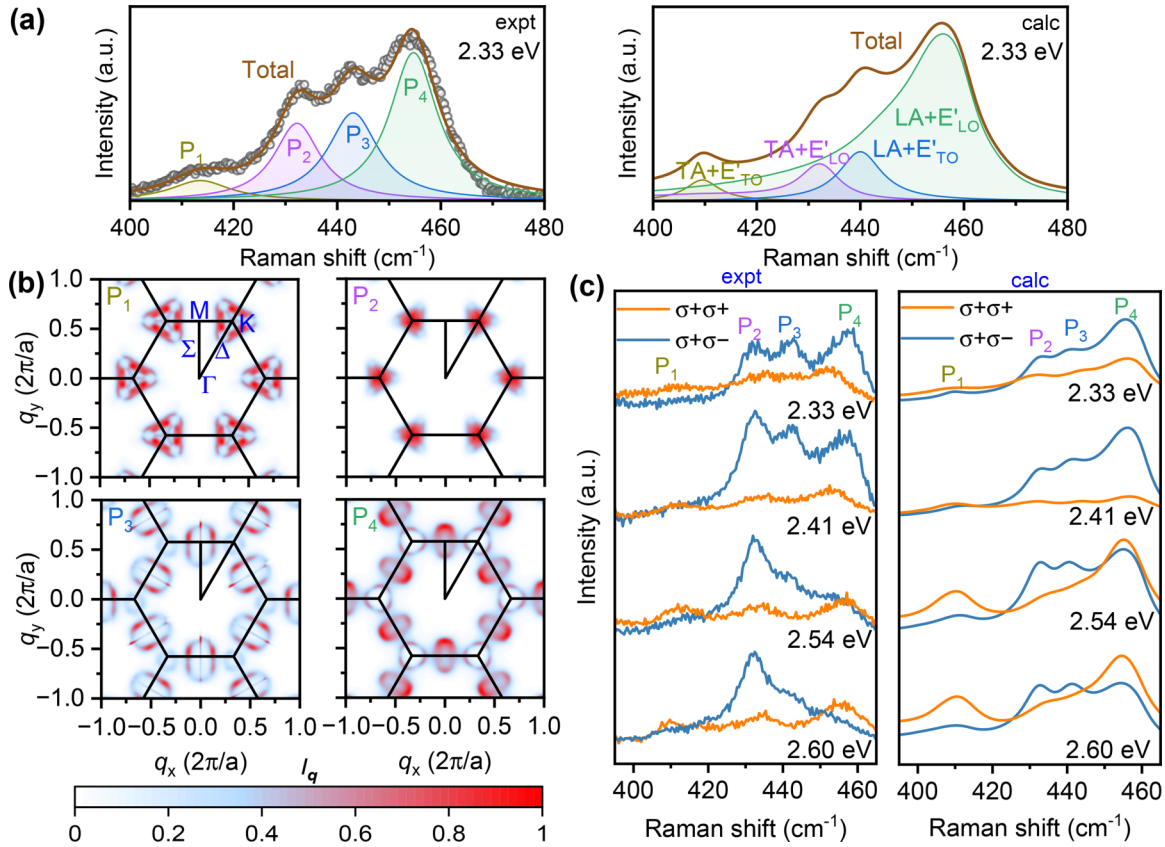


FIG. 2. (a) Mode-dependent Raman spectra at laser excitation energy $E_L = 2.33$ eV: experiment (left) and calculation (right). (b) Normalized $\boldsymbol{q}$-dependent Raman spectra for four bands $P_i$ ($i = 1, 2, 3, 4$). The value of each $P_i$ is normalized by its corresponding maximum. (c) Circularly polarized Raman spectra for monolayer $MoSe_2$: experiment (left) and calculation (right). Orange and blue lines represent the helicity-conserved and helicity-changing geometries, respectively.

not discuss them here. Thus, we mainly focus on the seven principal bands denoted as $P_1$–$P_4$ and $S_1$–$S_3$ below.

### B. Analysis of $P_1 - P_4$ at $400 - 480\ cm^{-1}$

In Fig. 2(a), we plot the experimental and calculated mode-dependent Raman spectra of $P_1$–$P_4$ observed at 400–480 $cm^{-1}$ for $E_L = 2.33$ eV. For other $E_L$, we show Raman spectra in Fig. S4 of SM [40]. These four bands $P_1$–$P_4$ are assigned to combination modes involving acoustic and optical phonon branches as follows: (i) $P_1$: $TA + E'_{TO}$, (ii) $P_2$: $TA + E'_{LO}$, (iii) $P_3$: $LA + E'_{TO}$, and (iv) $P_4$: $LA + E'_{LO}$. In order to analyze the origin of $P_i$ in the phonon momentum space, we present $\boldsymbol{q}$-dependent Raman spectra of $P_i$ at $E_L = 2.33$ eV in Fig. 2(b). The dominant contributions to the Raman intensities of $P_1$ and $P_2$ arise from wave vectors around the K point, whereas those of $P_3$ and $P_4$ come from the region around the M point. The $\boldsymbol{q}$-dependent spectra for other excitation energies are shown in Fig. S5 of SM [40] and are consistent with the current results.

Since we have a clear phonon assignment for each $P_i$, the helicity-dependent behaviors can be systematically determined by the analysis of space-group theory. With the help of the Bilbao crystallographic server [41], we decompose the direct product of Irreps for a pair of two phonons at the high symmetry points into a Γ star for each $P_i$ in Table II. If Γ star contains $A'_1$ ($E'$), we expect that the Raman spectra show helicity-conserved (helicity-changing) behavior. The results reveal the following: (i) the Raman-active Irrep in Γ star of $P_1$ is $A'_1$, which is helicity conserved; (ii) the Raman-active Irreps in Γ star of $P_2$ and $P_3$ are $E'$, which is helicity changing; (iii) the Raman-active Irreps in Γ star of $P_4$ are both $A'_1$ and $E'$, which have both helicity-conserved and helicity-changing components (i.e., hybrid symmetry). The predictions are consistent with experimentally observed helicity-dependent Raman spectra as shown in Fig. 2(c). The observed helicity-dependent behaviors confirm the following points: (i) $P_1$ and $P_2$ are helicity conserved, while $P_3$ exhibits helicity-changing character; (ii) $P_4$ exhibits a $E_L$-dependent helicity transition from changing to conserving helicity.

TABLE II. Decomposing the direct product of Irreps of wave vector stars into the combination of Irreps in Γ star for $P_i$. The red mark in the last column represents the Raman-active mode in the backscattering geometry.

| Band | Assignment | Direct product | Decomposition to Γ star |
|---|---|---|---|
| $P_1$ | $TA + E'_{TO}$ | ${}^2E' \otimes {}^2E'$ (K) | $A'_1 \oplus A'_2$ |
| $P_2$ | $TA + E'_{LO}$ | ${}^2E' \otimes A'$ (K) | $E'$ |
| $P_3$ | $LA + E'_{TO}$ | $A_1 \otimes B_1$ (M) | $A'_2 \oplus E'$ |
| $P_4$ | $LA + E'_{LO}$ | $A_1 \otimes A_1$ (M) | $A'_1 \oplus E'$ |

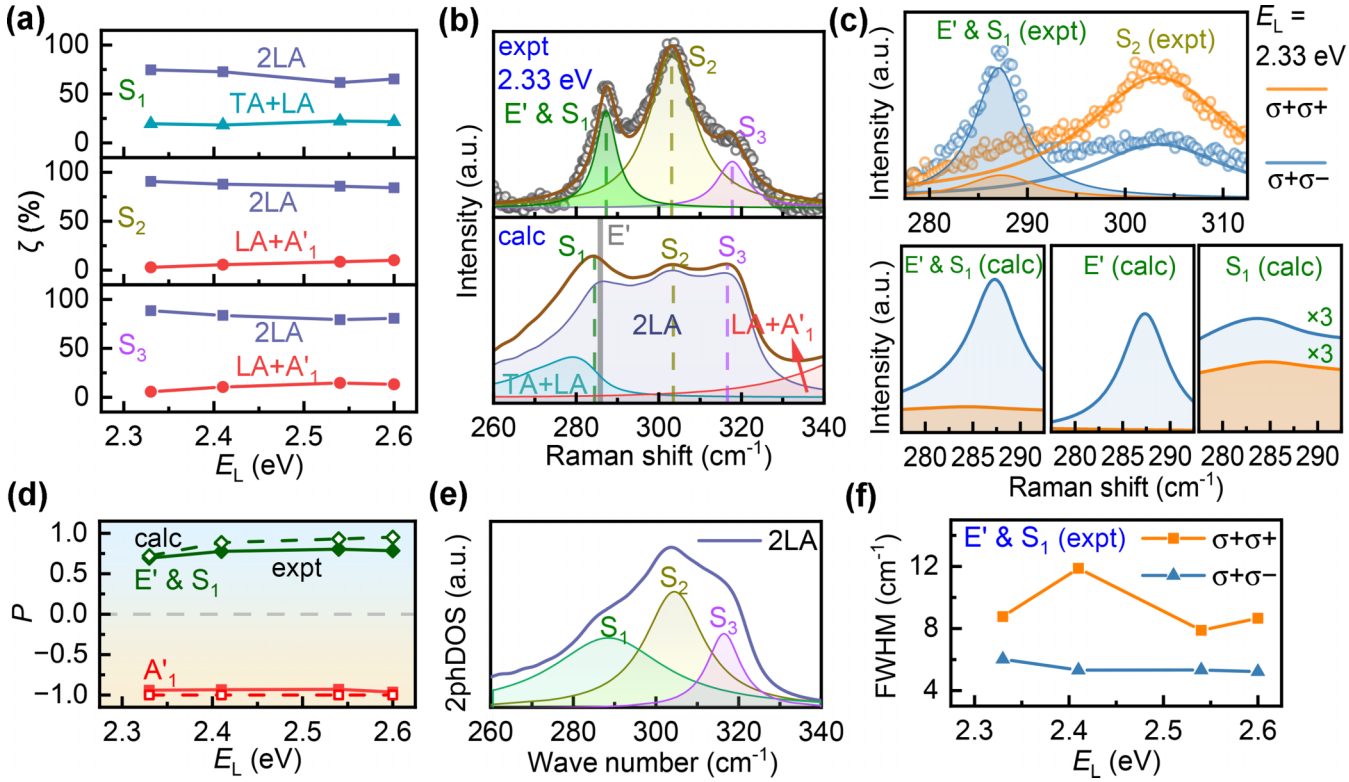


FIG. 3. (a) Weight of contribution to Raman intensity ($\zeta$) as a function of $E_L$ for each $S_i$. (b) Mode-dependent Raman spectra at $E_L = 2.33$ eV: experiment (top) and calculation (bottom). The vertical dark gray bar in bottom panel indicates the calculated peak position of first-order mode E′. (c) Circularly polarized Raman spectra for monolayer $MoSe_2$ at $E_L = 2.33$ eV. The orange and blue lines represent the helicity-conserving and helicity-changing geometries, respectively. (d) Polarization degree $P$ as a function of $E_L$ for $A_1'$ (red lines) and E′ & $S_1$ (green lines). Solid and dashed lines represent experimental and calculated results, respectively. (e) Calculated two-phonon density of states (2phDOS) for 2LA mode that is fitted by three Lorentzian functions. (f) Experimental full width at half-maxima (FWHM) of E′ and $S_1$ band as a function of $E_L$ for the $\sigma^+\sigma^+$ (orange line) and $\sigma^+\sigma^-$ (blue line) geometries.

### C. Analysis of $S_1$–$S_3$ at 280–320 cm$^{-1}$

The analysis of the $S_1$–$S_3$ bands at 280–320 cm$^{-1}$ can be similarly done. In Fig. 3(a), we show the top two contributions to the Raman intensity ($\zeta$) for the candidate two-phonon modes, revealing that the 2LA overtone mode dominates the Raman intensity for the three bands. In contrast, the combination modes TA + LA and LA + $A_1'$ exhibit trivial contributions. To confirm the assignment, as shown in Fig. 3(b), we compare the calculated mode-dependent DRR spectra for $E_L = 2.33$ eV with the experimental data. For the direct analysis of DRR modes, the calculated first-order mode E′ Raman intensity profile is subtracted in the bottom panel of Fig. 3(b), leaving the peak position of first-order mode E′ identified by the thin dark gray bar. The contributions of TA + LA and LA + $A_1'$ manifest solely the peak tails at adjacent wave numbers. This evidence conclusively assigns all three bands to 2LA.

Notably, the second-order mode $S_1$ in Fig. 3(b) exhibits spectral overlap with the first-order mode E′. In Fig. 3(c), we compare the experimental and calculated, helicity-dependent Raman spectra for the superposition of E′ and $S_1$ (labeled as E′ & $S_1$) at $E_L = 2.33$ eV, with the isolated contributions of E′ and $S_1$ from the calculation separately. The Raman peaks emerge in both helicity-conserved and helicity-changing geometries. Although the helicity-changing signal is E′ dominant with a minor contribution from $S_1$, the helicity-conserved signal comes completely from the contribution of $S_1$. The helicity-dependent behaviors also show the hybrid symmetry of $S_1$ (i.e., having both A- and E-type components), directly demonstrating the superposition of E′ and $S_1$. In Fig. 3(d), we compare the experimental and calculated polarization degree $P$ for E′ & $S_1$, with another typical first-order mode $A_1'$ for comparison. Here, the polarization degree $P$ is defined as follows [42],

$$P = \frac{I(\sigma^+\sigma^-) - I(\sigma^+\sigma^+)}{I(\sigma^+\sigma^-) + I(\sigma^+\sigma^+)}, \tag{12}$$

where $I(\sigma^+\sigma^-)$ and $I(\sigma^+\sigma^+)$ denote the Raman intensities in the helicity-changing and helicity-conserved geometries, respectively. The positive and negative signs of $P$ represent helicity-changing and helicity-conserved mode dominating, respectively. In particular, the values of 1 and −1 represent typical E- and A-type symmetries, respectively. The calculation reproduces the experimental results satisfactorily. As shown in Fig. 3(d), the $A_1'$ band exhibits typical A-type symmetry, which is consistent with space-group theory analysis. In contrast, the value of $P$ for E′ & $S_1$ deviates from the typical E-type symmetry ($P = 1$) due to the contribution of $S_1$, which corroborates the hybrid symmetry of the overlapping modes. Furthermore, Fig. 3(f) presents the experimental full width at

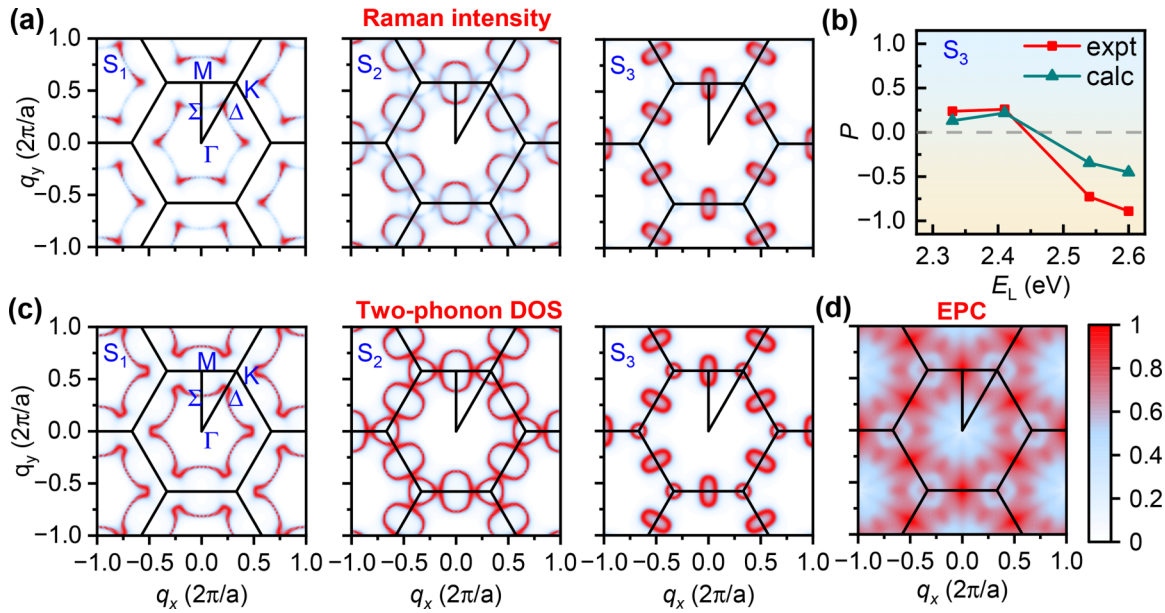


FIG. 4. (a) Normalized $\boldsymbol{q}$-dependent Raman spectra for $S_i$. (b) Polarization degree $P$ as a function of $E_L$ for the band $S_3$: experiment (red lines) and calculation (green lines). (c) Normalized $\boldsymbol{q}$-dependent two-phonon density of states (2phDOS). (d) Normalized $\boldsymbol{q}$-dependent electron-phonon coupling (EPC) strength $\lambda$ for LA phonon branch. The values in (a), (c), and (d) are normalized by their corresponding maximum, respectively, with sharing the same color bar in (d).

half-maxima (FWHM) of E′ & $S_1$ in the $\sigma^+\sigma^+$ and $\sigma^+\sigma^-$ geometries, which shows that FWHM of $\sigma^+\sigma^+$ is greater than that of $\sigma^+\sigma^-$. In general, a second-order mode has a relatively larger FWHM than a first-order mode [43,44]. Thus, this fact also supports that the second-order mode $S_1$ overlaps with the first-order mode E′.

Now, let us discuss the reason why the three peaks of $S_1$–$S_3$ appear, though all peaks are assigned by 2LA. In Fig. 3(e), we plot the 2phDOS for 2LA mode, which is expressed as follows,

$$\text{2phDOS}(\omega) = \sum_{\boldsymbol{q},\mu,\nu} \delta(\omega - \omega_{\boldsymbol{q},\mu} - \omega_{\boldsymbol{q},\nu}), \tag{13}$$

where $\omega_{\mu,\boldsymbol{q}}$ and $\omega_{\nu,\boldsymbol{q}}$ denote the angular frequencies corresponding to $\mu$th and $\nu$th phonon modes. The 2phDOS of 2LA can be fitted by three Lorentzian functions, with the fitted peak positions exhibiting a one-to-one correspondence to those of $S_i$ bands. This suggests that $S_1$–$S_3$ comes from the different $\boldsymbol{q}$ points on the phonon dispersion of LA mode.

In Fig. 4(a), we plot the $\boldsymbol{q}$-dependent Raman spectra of $S_1$–$S_3$ at $E_L = 2.33$ eV for showing the contribution of Raman spectra explicitly. The dominant $\boldsymbol{q}$ points that contribute to Raman intensities for $S_1$, $S_2$, and $S_3$ are identified as Λ (ΓK), Σ (ΓM), and around the M point, respectively. This result demonstrates that double-resonance Raman scattering events for 2LA occur in the three different positions of phonon wave vector space.

When we compare Figs. 2(b) and 4(a), $\boldsymbol{q}$ dependence for $S_3$ and $P_4$ are almost identical. Since the decomposed Irreps at the Γ star for $S_3$ and $P_4$ are similar, too, we expect the same helicity dependence. As shown in Figs. 4(b) and 2(c), $S_3$ and $P_4$ exhibit a consistent transition in helicity selection rules: helicity-changing behavior dominates at lower excitation energies ($E_L \leqslant 2.41$ eV), while helicity-conserved processes prevail at higher excitation energies ($E_L \geqslant 2.54$ eV). These helicity behaviors further corroborate our assignment. Moreover, the $\boldsymbol{q}$-dependent Raman spectra of other excitation energies are given in Fig. S6 in the SM [40] and are consistent with the presented result. Thus, we discuss the behavior of $S_i$ at the phonon level. The $\boldsymbol{q}$-dependent 2phDOS in Fig. 4(c) can reproduce $\boldsymbol{q}$-dependent Raman spectra well, except the $\boldsymbol{q}$ points around the K point for $S_3$. To explain the deviation caused by 2phDOS, we calculated $\boldsymbol{q}$-dependent EPC strength. The EPC strength [39,45] associated with a specific phonon mode $\mu$ and wave vector $\boldsymbol{q}$ within the double-delta approximation is expressed as follows,

$$\lambda_{\boldsymbol{q},\mu} = \frac{1}{N_F \omega_{\boldsymbol{q},\mu}} \sum_{mn,\boldsymbol{k}} |\mathcal{M}_{mn,\mu}(\boldsymbol{k},\boldsymbol{q})|^2 \times \delta(E_{n,\boldsymbol{k}} - E_F)\delta(E_{m,\boldsymbol{k}+\boldsymbol{q}} - E_F), \tag{14}$$

where $N_F$ is the density of states per spin at the Fermi level $E_F$, and $\mathcal{M}_{mn,\mu}(\boldsymbol{k},\boldsymbol{q})$ and $E_{n,\boldsymbol{k}}$ are the EPC matrix elements [46,47] and the electron band energy, respectively. In Fig. 4(d), we present $\boldsymbol{q}$-dependent EPC strength of the LA phonon branch. A critical suppression of EPC strength emerges around the K point, which directly explains the low Raman intensity within this region of phonon wave vector space.

In this paper, we achieve precise assignment of the DRR modes observed in monolayer $MoSe_2$, using first-principles calculations, helicity selection rule, and space-group theory analysis. Beyond assignment, analysis of the behavior of each scattering process pathway and its associated quantum interference effect is essential for the physics of the observed Raman spectra. The decomposition of the total Raman spectra into constituent scattering pathways (Fig. S7 of SM [40]) shows that first-order modes $A_1'$ and E′ exhibit destructive and

constructive interferences between the $e$ and $h$ paths, respectively. The interference effect for the $A_1'$ and $E'$ is independent of $E_L$. In contrast, all second-order modes exhibit constructive interference among the four pathways, with *eh* and *he* processes contributing nearly equally to the Raman intensity. Notably, for the modes below $500\,cm^{-1}$, the contribution of *ee* process is minor at $E_L \leqslant 2.41\,eV$, but becomes dominant at $E_L \geqslant 2.54\,eV$. While we present these key observations here, a detailed mechanistic discussion of these interference effects is beyond the scope of this work and warrants further exploration.

## IV. CONCLUSION

In summary, we have presented the experimental and calculated Raman spectra for monolayer $MoSe_2$ at four laser excitation energies resonant with the C exciton, where 16 second-order Raman modes were observed. The mode and phonon contributions are quantitatively assigned by using the first-principles calculation. Focusing on the bands $S_i$ $(i = 1, 2, 3)$ at 280–320 $cm^{-1}$ and $P_i$ $(i = 1, 2, 3, 4)$ at 400–480 $cm^{-1}$ involving acoustic phonon branches, we discuss their detailed assignments and phonon behaviors. Contrary to previous reports suggesting higher-order modes, we assign the bands $P_i$ to the combination modes of TA (LA) and $E'_{TO}$ ($E'_{LO}$). This assignment is supported by space-group theory analysis and helicity-dependent Raman spectra. For bands $S_i$, all bands are assigned to the same 2LA mode but originating from different $\boldsymbol{q}$ points, which is explained by the combination of two-phonon density of states and electron-phonon coupling. Furthermore, we reveal the superposition of first-order mode $E'$ and second-order mode $S_1$. Our study resolves the controversy regarding second-order mode assignments in monolayer $MoSe_2$ and provides a comprehensive understanding of the physics behind the second-order Raman bands.

## ACKNOWLEDGMENTS

We acknowledge the support from the National Key R&D Program of China (2022YFA1203900), National Natural Science Foundation of China (Grants No. 12404213, No. 52031014, No. 12322401, No. 12127807, and No. 12393832), the Strategic Priority Research Program of CAS (Grant No. XDB0460000), CAS Key Research Program of Frontier Sciences (Grant No. ZDBS-LY-SLH004), Beijing Nova Program (Grant No. 20230484301), Youth Innovation Promotion Association, Chinese Academy of Sciences (No. 2023125). R.S. acknowledges a JSPS KAKENHI Grant (No. JP22H00283). N.T.H. acknowledges financial support from the Frontier Research Institute for Interdisciplinary Sciences, Tohoku University. The simulation work was partly carried out at National Supercomputer Center in Tianjin, China, and the calculations were performed on TianHe-1(A). We gratefully acknowledge HZWTECH for providing computation facilities.

## DATA AVAILABILITY

The data that support the findings of this article are not publicly available. The data are available from the authors upon reasonable request.

[1] A. C. Ferrari, J. C. Meyer, V. Scardaci, C. Casiraghi, M. Lazzeri, F. Mauri, S. Piscanec, D. Jiang, K. S. Novoselov, S. Roth, and A. K. Geim, Raman spectrum of graphene and graphene layers, Phys. Rev. Lett. **97**, 187401 (2006).

[2] M. A. Pimenta, G. Dresselhaus, M. S. Dresselhaus, L. G. Cançado, A. Jorio, and R. Saito, Studying disorder in graphite-based systems by Raman spectroscopy, Phys. Chem. Chem. Phys. **9**, 1276 (2007).

[3] P. Venezuela, M. Lazzeri, and F. Mauri, Theory of double-resonant Raman spectra in graphene: Intensity and line shape of defect-induced and two-phonon bands, Phys. Rev. B **84**, 035433 (2011).

[4] P.-H. Tan, ed., *Raman Spectroscopy of Two-Dimensional Materials*, Springer Series in Materials Science (World Scientific, Singapore, 2019), Vol. 276.

[5] R. Saito, N. T. Hung, T. Yang, J. Huang, H.-L. Liu, D. P. Gulo, S. Han, and L. Tong, Deep-ultraviolet and helicity-dependent Raman spectroscopy for carbon nanotubes and 2D materials, Small **21**, 2308558 (2024).

[6] R. Saito, A. Jorio, A. G. Souza Filho, G. Dresselhaus, M. S. Dresselhaus, and M. A. Pimenta, Probing phonon dispersion relations of graphite by double resonance Raman scattering, Phys. Rev. Lett. **88**, 027401 (2001).

[7] D. L. Mafra, G. Samsonidze, L. M. Malard, D. C. Elias, J. C. Brant, F. Plentz, E. S. Alves, and M. A. Pimenta, Determination of LA and TO phonon dispersion relations of graphene near the Dirac point by double resonance Raman scattering, Phys. Rev. B **76**, 233407 (2007).

[8] M. Yamamoto, S. T. Wang, M. Ni, Y.-F. Lin, S.-L. Li, S. Aikawa, W.-B. Jian, K. Ueno, K. Wakabayashi, and K. Tsukagoshi, Strong enhancement of Raman scattering from a bulk-inactive vibrational mode in few-layer $MoTe_2$, ACS Nano **8**, 3895 (2014).

[9] S.-Y. Chen, C. Zheng, M. S. Fuhrer, and J. Yan, Helicity-resolved Raman scattering of $MoS_2$, $MoSe_2$, $WS_2$, and $WSe_2$ atomic layers, Nano Lett. **15**, 2526 (2015).

[10] H.-L. Liu, H. Guo, T. Yang, Z. Zhang, Y. Kumamoto, C.-C. Shen, Y.-T. Hsu, L.-J. Li, R. Saito, and S. Kawata, Anomalous lattice vibrations of monolayer $MoS_2$ probed by ultraviolet Raman scattering, Phys. Chem. Chem. Phys. **17**, 14561 (2015).

[11] H. Guo, T. Yang, M. Yamamoto, L. Zhou, R. Ishikawa, K. Ueno, K. Tsukagoshi, Z. Zhang, M. S. Dresselhaus, and R. Saito, Double resonance Raman modes in monolayer and few-layer $MoTe_2$, Phys. Rev. B **91**, 205415 (2015).

[12] B. R. Carvalho, Y. Wang, S. Mignuzzi, D. Roy, M. Terrones, C. Fantini, V. H. Crespi, L. M. Malard, and M. A. Pimenta, Intervalley scattering by acoustic phonons in two-dimensional $MoS_2$ revealed by double-resonance Raman spectroscopy, Nat. Commun. **8**, 14670 (2017).

[13] P. Soubelet, A. E. Bruchhausen, A. Fainstein, K. Nogajewski, and C. Faugeras, Resonance effects in the Raman scattering of monolayer and few-layer $MoSe_2$, Phys. Rev. B **93**, 155407 (2016).

[14] I. Bilgin, A. S. Raeliarijaona, M. C. Lucking, S. C. Hodge, A. D. Mohite, A. de Luna Bugallo, H. Terrones, and S. Kar, Resonant Raman and exciton coupling in high-quality single crystals of atomically thin molybdenum diselenide grown by vapor-phase chalcogenization, ACS Nano **12**, 740 (2018).

[15] S. Sotgiu, T. Venanzi, F. Macheda, E. Stellino, M. Ortolani, P. Postorino, and L. Baldassarre, Raman scattering with infrared excitation resonant with the $MoSe_2$ indirect band gap, Phys. Rev. B **106**, 085204 (2022).

[16] R. Liu, L.-H. Li, Y. Zhang, J. Huang, M.-L. Lin, N. T. Hung, Z. Wang, Z. Zhang, R. Saito, P.-H. Tan, and T. Yang, Helicity selection rule of double resonance Raman spectra for monolayer $MoSe_2$, Phys. Rev. B **110**, 245422 (2024).

[17] S. Mignuzzi, A. J. Pollard, N. Bonini, B. Brennan, I. S. Gilmore, M. A. Pimenta, D. Richards, and D. Roy, Effect of disorder on Raman scattering of single-layer $MoS_2$, Phys. Rev. B **91**, 195411 (2015).

[18] Q. Qian, Z. Zhang, M. Hua, G. Tang, J. Lei, F. Lan, Y. Xu, R. Yan, and K. J. Chen, Enhanced dielectric deposition on single-layer $MoS_2$ with low damage using remote $N_2$ plasma treatment, Nanotechnol. **28**, 175202 (2017).

[19] A. Berkdemir, H. R. Gutiérrez, A. R. Botello-Méndez, N. Perea-López, A. L. Elías, C.-I. Chia, B. Wang, V. H. Crespi, F. López-Urías, J.-C. Charlier, H. Terrones, and M. Terrones, Identification of individual and few layers of $WS_2$ using Raman spectroscopy, Sci. Rep. **3**, 1755 (2013).

[20] K. F. Mak, K. He, J. Shan, and T. F. Heinz, Control of valley polarization in monolayer $MoS_2$ by optical helicity, Nat. Nanotechnol. **7**, 494 (2012).

[21] X. Xi, L. Zhao, Z. Wang, H. Berger, L. Forró, J. Shan, and K. F. Mak, Strongly enhanced charge-density-wave order in monolayer $NbSe_2$, Nat. Nanotechnol. **10**, 765 (2015).

[22] K. Kim, J.-U. Lee, D. Nam, and H. Cheong, Davydov splitting and excitonic resonance effects in Raman spectra of few-layer $MoSe_2$, ACS Nano **10**, 8113 (2016).

[23] K. Okubo and S.-i. Tamura, Two-phonon density of states and anharmonic decay of large-wave-vector LA phonons, Phys. Rev. B **28**, 4847 (1983).

[24] J. Huang, H. Guo, L. Zhou, S. Zhang, L. Tong, R. Saito, T. Yang, and Z. Zhang, First-principles calculations of double resonance Raman spectra for monolayer $MoTe_2$, Phys. Rev. B **105**, 235401 (2022).

[25] J. Huang, R. Liu, Y. Zhang, H. T. Nguyen, H. Guo, R. Saito, and T. Yang, $QR^2$-code: An open-source program for double resonance Raman spectra, arXiv:2505.10041.

[26] Y. Zhang, R. Liu, J. Huang, N. Tuan Hung, R. Saito, T. Yang, and Z. Zhang, DUV double-resonant Raman spectra and interference effect in graphene: First-principles calculations, J. Raman Spectrosc. **56**, 316 (2025).

[27] J. Huang, Z. Liu, T. Yang, and Z. Zhang, New selection rule of resonant Raman scattering in $MoS_2$ monolayer under circular polarization, J. Mater. Sci. Technol. **102**, 132 (2022).

[28] W. Wang, R. Liu, Y. Zhang, H. Guo, J. Huang, Z. Liu, H. Zhao, K. Wang, B. Zhao, and T. Yang, Anomalous lattice vibration in monolayer $MoS_2$ induced by DUV laser: A first-principles investigation, Chin. Phys. B **34**, 066301 (2025).

[29] Y. Pang, J. Huang, T. Yang, and Z. Zhang, Accurate assignment of double resonant Raman bands in Janus MoSSe monolayer from first-principles calculations, J. Mater. Sci. Technol. **131**, 82 (2022).

[30] S. Zhang, J. Huang, Y. Yu, S. Wang, T. Yang, Z. Zhang, L. Tong, and J. Zhang, Quantum interference directed chiral Raman scattering in two-dimensional enantiomers, Nat. Commun. **13**, 1254 (2022).

[31] D. Nam, J.-U. Lee, and H. Cheong, Excitation energy dependent Raman spectrum of $MoSe_2$, Sci. Rep. **5**, 17113 (2015).

[32] J. L. Birman, Space group selection rules: Diamond and zinc blende, Phys. Rev. **127**, 1093 (1962).

[33] J. L. Birman, Theory of infrared and Raman processes in crystals: Selection rules in diamond and zincblende, Phys. Rev. **131**, 1489 (1963).

[34] T. Livneh and J. E. Spanier, A comprehensive multiphonon spectral analysis in $MoS_2$, 2D Mater. **2**, 035003 (2015).

[35] P. Giannozzi, S. Baroni, N. Bonini, M. Calandra, R. Car, C. Cavazzoni, D. Ceresoli, G. L. Chiarotti, M. Cococcioni, I. Dabo, A. D. Corso, S. D. Gironcoli, S. Fabris, G. Fratesi, R. Gebauer, U. Gerstmann, C. Gougoussis, A. Kokalj, M. Lazzeri, L. Martin-Samos, N. Marzari, F. Mauri, R. Mazzarello, S. Paolini, A. Pasquarello, L. Paulatto, C. Sbraccia, S. Scandolo, G. Sclauzero, A. P. Seitsonen, A. Smogunov, P. Umari, and R. M. Wentzcovitch, QUANTUM ESPRESSO: a modular and open-source software project for quantum simulations of materials, J. Phys.: Condens. Matter **21**, 395502 (2009).

[36] G. Theurich and N. A. Hill, Self-consistent treatment of spin-orbit coupling in solids using relativistic fully separable *ab initio* pseudopotentials, Phys. Rev. B **64**, 073106 (2001).

[37] P. E. Blöchl, Projector augmented-wave method, Phys. Rev. B **50**, 17953 (1994).

[38] J. Noffsinger, F. Giustino, B. D. Malone, C.-H. Park, S. G. Louie, and M. L. Cohen, EPW: A program for calculating the electron-phonon coupling using maximally localized Wannier functions, Comput. Phys. Commun. **181**, 2140 (2010).

[39] S. Poncé, E. R. Margine, C. Verdi, and F. Giustino, EPW: Electron-phonon coupling, transport and superconducting properties using maximally localized Wannier functions, Comput. Phys. Commun. **209**, 116 (2016).

[40] See Supplemental Material at http://link.aps.org/supplemental/10.1103/vvkp-9sth for (i) convergence test for calculated Raman spectra, (ii) experimental Raman spectra at low temperature, (iii) additional Raman spectra and analysis at $E_L =$ 2.41, 2.54 and 2.60 eV, and (iv) decomposition of total Raman spectra into different scattering processes, which includes Refs. [48,49].

[41] M. I. Aroyo, A. Kirov, C. Capillas, J. M. Perez-Mato, and H. Wondratschek, Bilbao crystallographic server II: Representations of crystallographic point groups and space groups, Acta Cryst. A **62**, 115 (2006).

[42] Y. Zhao, B. Xu, L. Tong, and J. Zhang, The helicity of Raman scattered light: principles and applications in two-dimensional materials, Sci. China Chem. **65**, 269 (2022).

[43] R. Saito, A. Grüneis, G. G. Samsonidze, V. W. Brar, G. Dresselhaus, M. S. Dresselhaus, A. Jorio, L. G. Cançado, C. Fantini, M. A. Pimenta, and A. G. Souza Filho, Double resonance Raman spectroscopy of single wall carbon nanotubes, New J. Phys. **5**, 157 (2003).

[44] R. Saito, M. Hofmann, G. Dresselhaus, A. Jorio, and M. S. Dresselhaus, Raman spectroscopy of graphene and carbon nanotubes, Adv. Phys. **60**, 413 (2011).

[45] F. Giustino, Electron-phonon interactions from first principles, Rev. Mod. Phys. **89**, 015003 (2017).

[46] A. Grüneis, R. Saito, G. G. Samsonidze, T. Kimura, M. A. Pimenta, A. Jorio, A. G. S. Filho, G. Dresselhaus, and M. S. Dresselhaus, Inhomogeneous optical absorption around the *K* point in graphite and carbon nanotubes, Phys. Rev. B **67**, 165402 (2003).

[47] J. Jiang, R. Saito, A. Grüneis, S. G. Chou, G. G. Samsonidze, A. Jorio, G. Dresselhaus, and M. S. Dresselhaus, Intensity of the resonance Raman excitation spectra of single-wall carbon nanotubes, Phys. Rev. B **71**, 205420 (2005).

[48] P. H. Tan, Y. M. Deng, and Q. Zhao, Temperature-dependent Raman spectra and anomalous Raman phenomenon of highly oriented pyrolytic graphite, Phys. Rev. B **58**, 5435 (1998).

[49] K. Gołasa, M. Grzeszczyk, P. Leszczyński, C. Faugeras, A. A. L. Nicolet, A. Wysmołek, M. Potemski, and A. Babiński, Multiphonon resonant Raman scattering in $MoS_2$, Appl. Phys. Lett. **104**, 092106 (2014).

# Supplemental Information: Characterizing second-order Raman modes in monolayer $MoSe_2$

Renhui Liu[1,2], Lin-Han Li[3,4], Ye Zhang[1,2], Jianqi Huang[5],* Miao-Ling Lin[3,4], Nguyen Tuan Hung[6], Huaihong Guo[7],† Zhenhua Wang[1,2], Zhidong Zhang[1,2], Riichiro Saito[8], Ping-Heng Tan[3,4],‡ and Teng Yang[1,2]§

[1] *School of Materials Science and Engineering, University of Science and Technology of China, Shenyang 110016, China*
[2] *Shenyang National Laboratory for Materials Science, Institute of Metal Research, Chinese Academy of Sciences, Shenyang 110016, China*
[3] *State Key Laboratory of Semiconductor Physics and Chip Technologies, Institute of Semiconductors, Chinese Academy of Sciences, Beijing 100083, China*
[4] *Center of Materials Science and Optoelectronics Engineering, University of Chinese Academy of Sciences, Beijing 100049, China*
[5] *Liaoning Academy of Materials, Shenyang 110167, China*
[6] *Frontier Research Institute for Interdisciplinary Sciences, Tohoku University, Sendai 980-8578, Japan*
[7] *College of Sciences, Liaoning Petrochemical University, Fushun 113001, China and*
[8] *Department of Physics, Tohoku University, Sendai 980-8578, Japan*

* jqhuang@lam.ln.cn
† hhguo@alum.imr.ac.cn
‡ phtan@semi.ac.cn
§ yanghaiteng@msn.com

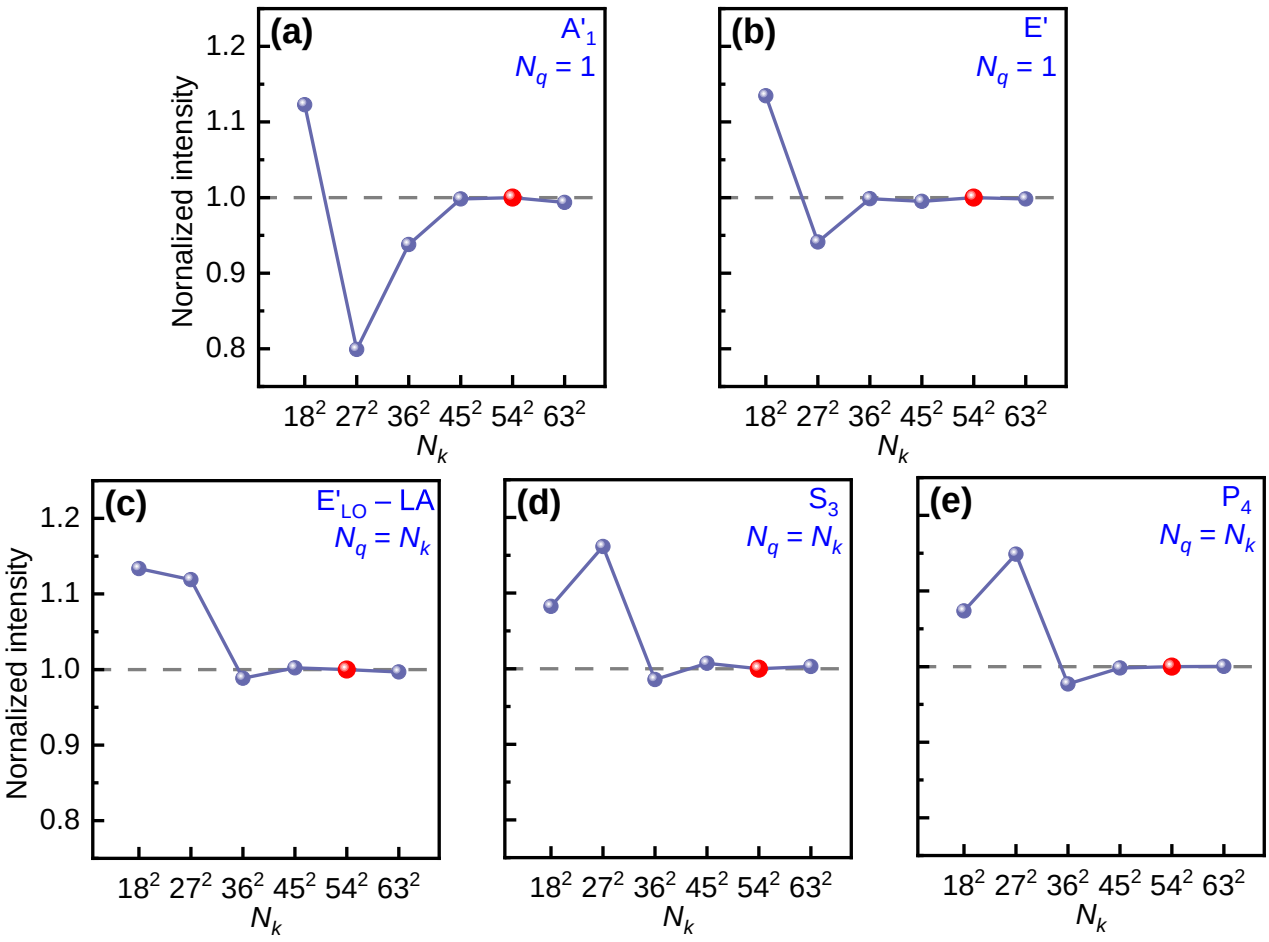


FIG. S1. Convergence test for calculated Raman spectra at $E_{\mathrm{L}} = 2.33$ eV: normalized intensity as a function of the number of interpolation $\boldsymbol{k}$ points $N_{\boldsymbol{k}}$ for (a) $\mathrm{A}_1'$, (b) $\mathrm{E}'$, (c) $\mathrm{E}'_{\mathrm{LO}} - \mathrm{LA}$, (d) $\mathrm{S}_3$, and (e) $\mathrm{P}_4$ modes. Top panels (a, b) show first-order modes, with the number of interpolation $\boldsymbol{q}$ point $N_{\boldsymbol{q}} = 1$. Bottom panels (c, d, e) show second-order modes, with $N_{\boldsymbol{q}} = N_{\boldsymbol{k}}$. The intensity for each panel is normalized by its corresponding value computed using a $54 \times 54$ $\boldsymbol{k}$-mesh.

In Fig. S1, we present the convergence test for two typical first-order modes ($\mathrm{A}_1'$ and $\mathrm{E}'$) and three second-order modes ($\mathrm{E}'_{\mathrm{LO}} - \mathrm{LA}$, $\mathrm{S}_3$, and $\mathrm{P}_4$). The intensity for each panel is normalized by its corresponding value computed using a $54 \times 54$ $\boldsymbol{k}$-mesh. For first-order modes, we adopt the number of interpolation $\boldsymbol{q}$ point $N_{\boldsymbol{q}} = 1$ for the $\Gamma$ point. For second-order modes, $N_{\boldsymbol{q}}$ shares the value of interpolation $\boldsymbol{k}$ points $N_{\boldsymbol{k}}$. The data demonstrate clear convergence for both first- and second-order modes at $N_{\boldsymbol{k}} \geqslant 54 \times 54$, validating our choice of meshes.

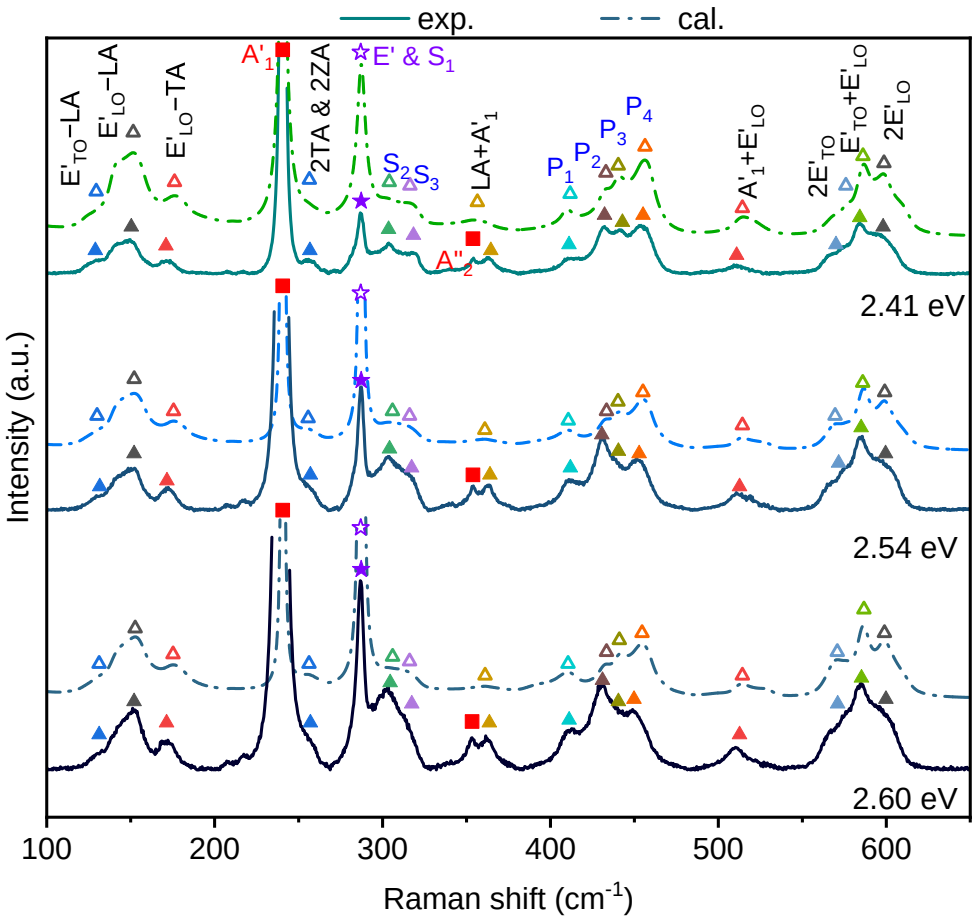


FIG. S2. Raman spectra of monolayer $MoSe_2$ at laser energy $E_L$ = 2.41, 2.54, and 2.60 eV: Experiment (solid lines) and calculation (dashed lines). Si peak is subtracted in the experimental Raman spectra. Triangle and star denote second-order mode and superposition of first-order mode E′ and second-order mode $S_1$ (labeled E′ & $S_1$), respectively.

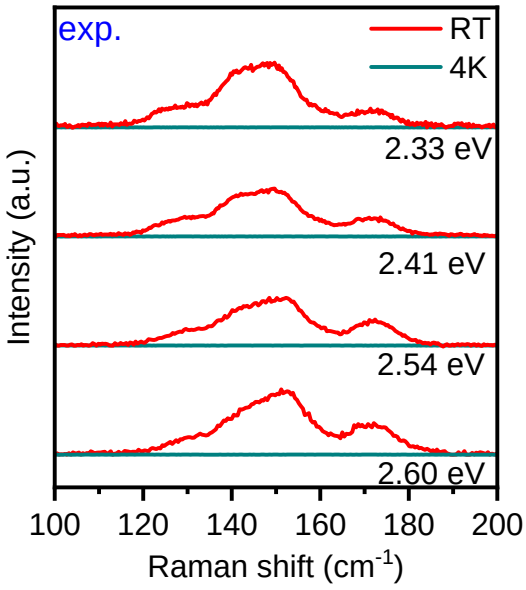


FIG. S3. Experimental Raman spectra of monolayer $MoSe_2$ at room temperature (RT, red lines) and 4 K (dark-cyan lines).

To validate the second-order combination modes involving coupled Stokes and anti-Stokes processes, temperature-dependent Raman spectra were systematically analyzed. As shown in Fig. S3, these modes exhibit pronounced intensity at room temperature but are entirely quenched at 4 K. The population of phonon $n_{\boldsymbol{q}}$ at frequency $\omega_{\boldsymbol{q}}$ follows the Bose-Einstein distribution as follows,

$$n_{\boldsymbol{q}}(\omega_{\boldsymbol{q}}, T) = \frac{1}{\exp\left(\frac{\hbar\omega_{\boldsymbol{q}}}{k_{\mathrm{B}}T}\right) - 1}, \tag{S1}$$

where $T$ and $k_{\mathrm{B}}$ represent temperature and Boltzmann's constant. Since the intensity of Stokes ($I_{\mathrm{S}}$) and anti-Stokes ($I_{\mathrm{AS}}$) processes are proportional to $n_{\boldsymbol{q}}$ and $n_{\boldsymbol{q}} + 1$ as follows,

$$I_{\mathrm{S}} \propto n_{\boldsymbol{q}}, \qquad I_{\mathrm{AS}} \propto n_{\boldsymbol{q}} + 1. \tag{S2}$$

The intensity of the anti-Stokes component $I_{\mathrm{AS}}$ decreases significantly at the low temperature. Thus, this thermal quenching directly demonstrates the existence of the anti-Stokes component in the second-order mode [1, 2], thereby providing experimental validation for our mode assignments.

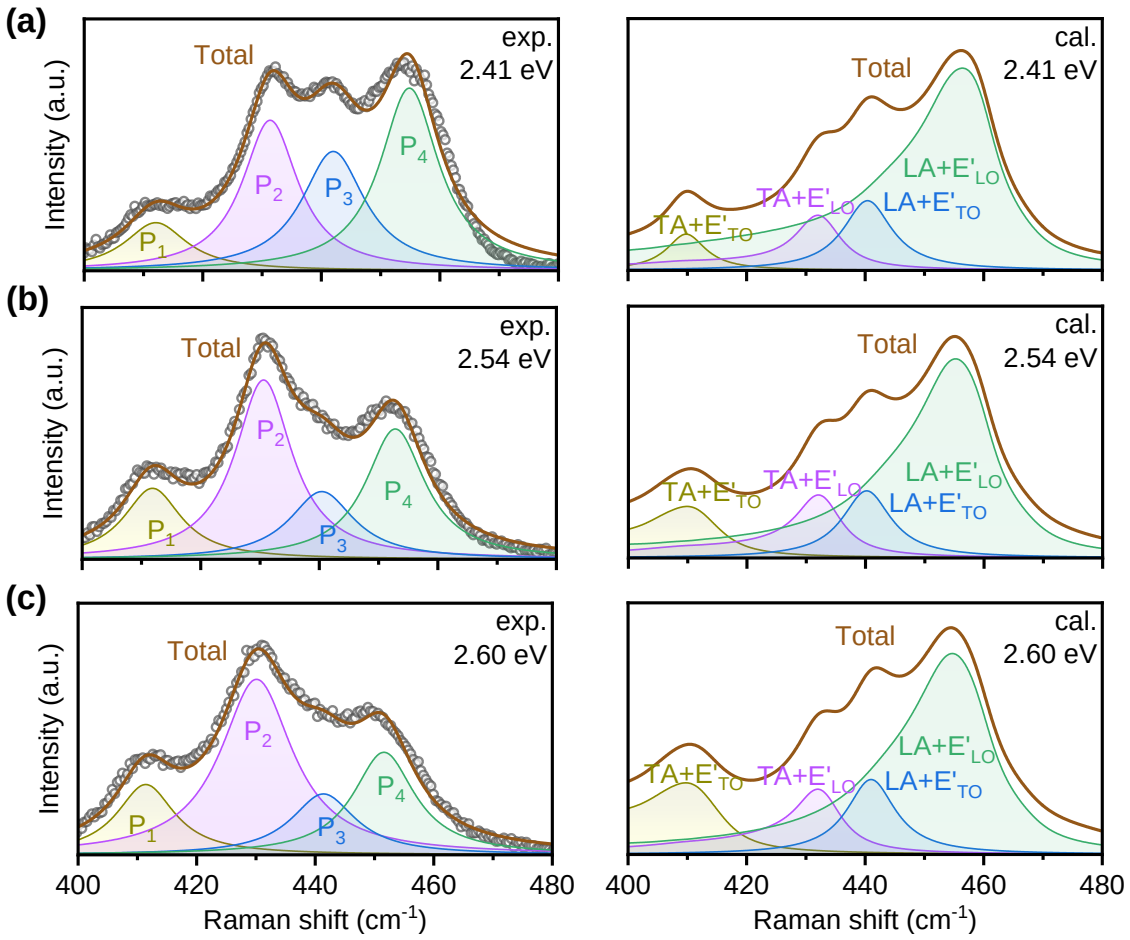


FIG. S4. Experimental (left) and calculated (right) mode-dependent Raman spectra of modes $P_i$ ($i = 1, 2, 3.4$) at $E_L$ = (a) 2.41, (b) 2.54, and (c) 2.60 eV. The brown solid line and gray circle represent the total Raman intensity and raw experimental data, respectively.

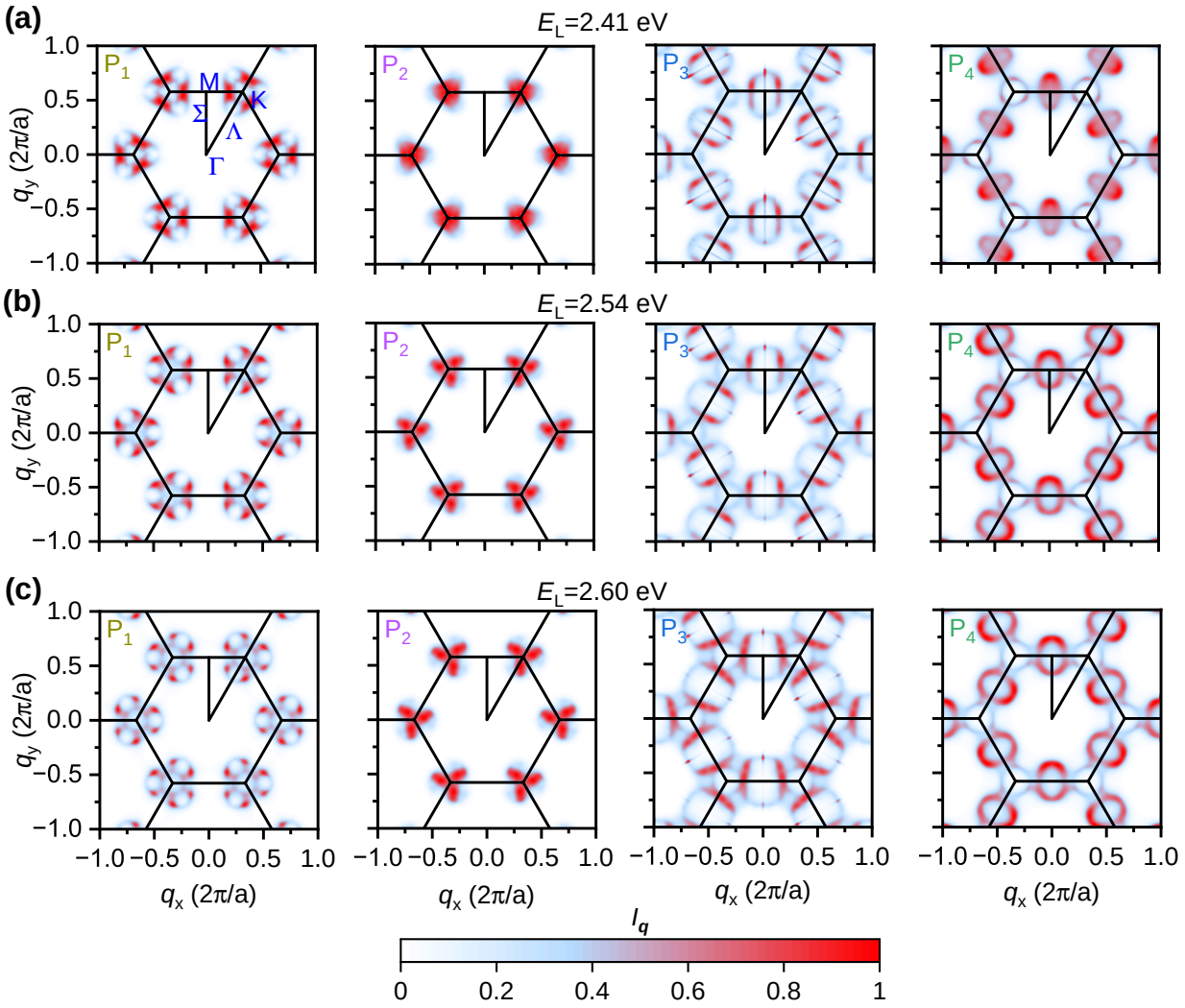


FIG. S5. The $\boldsymbol{q}$-dependent Raman spectra of modes $\mathrm{P}_i$ $(i = 1, 2, 3, 4)$ at $E_\mathrm{L}$ = (a) 2.41, (b) 2.54 and (c) 2.60 eV. The values are normalized by their corresponding maximum.

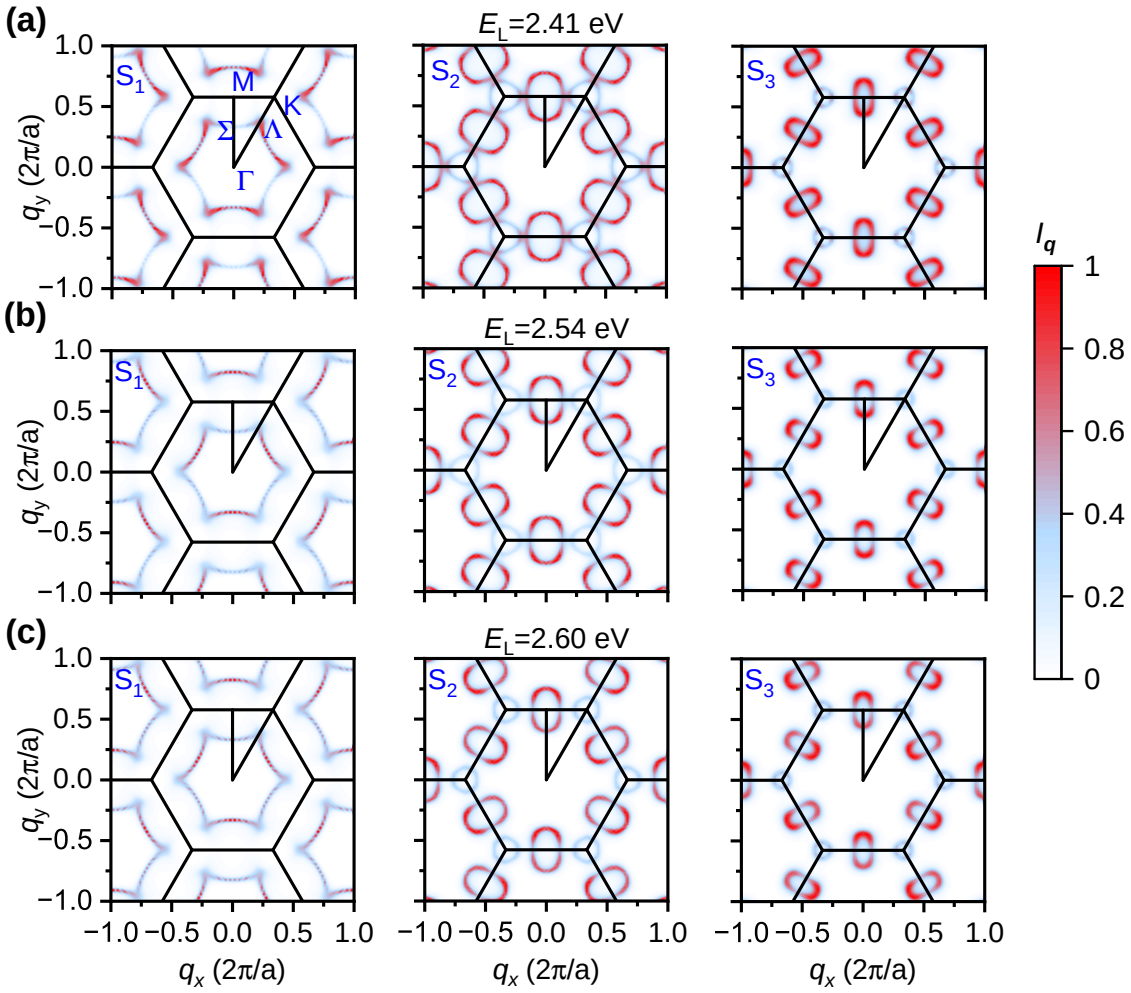


FIG. S6. The $\boldsymbol{q}$-dependent Raman spectra of modes $S_i$ $(i = 1, 2, 3)$ at $E_L$ = (a) 2.41, (b) 2.54 and (c) 2.60 eV. The values are normalized by their corresponding maximum.

As shown in Figs. S5 and S6, the $\boldsymbol{q}$ points that have a dominant contribution to the Raman intensity for each mode are nearly independent of $E_L$. It reveals the invariant assignment for the variation of $E_L$, which is also mentioned in the main text.

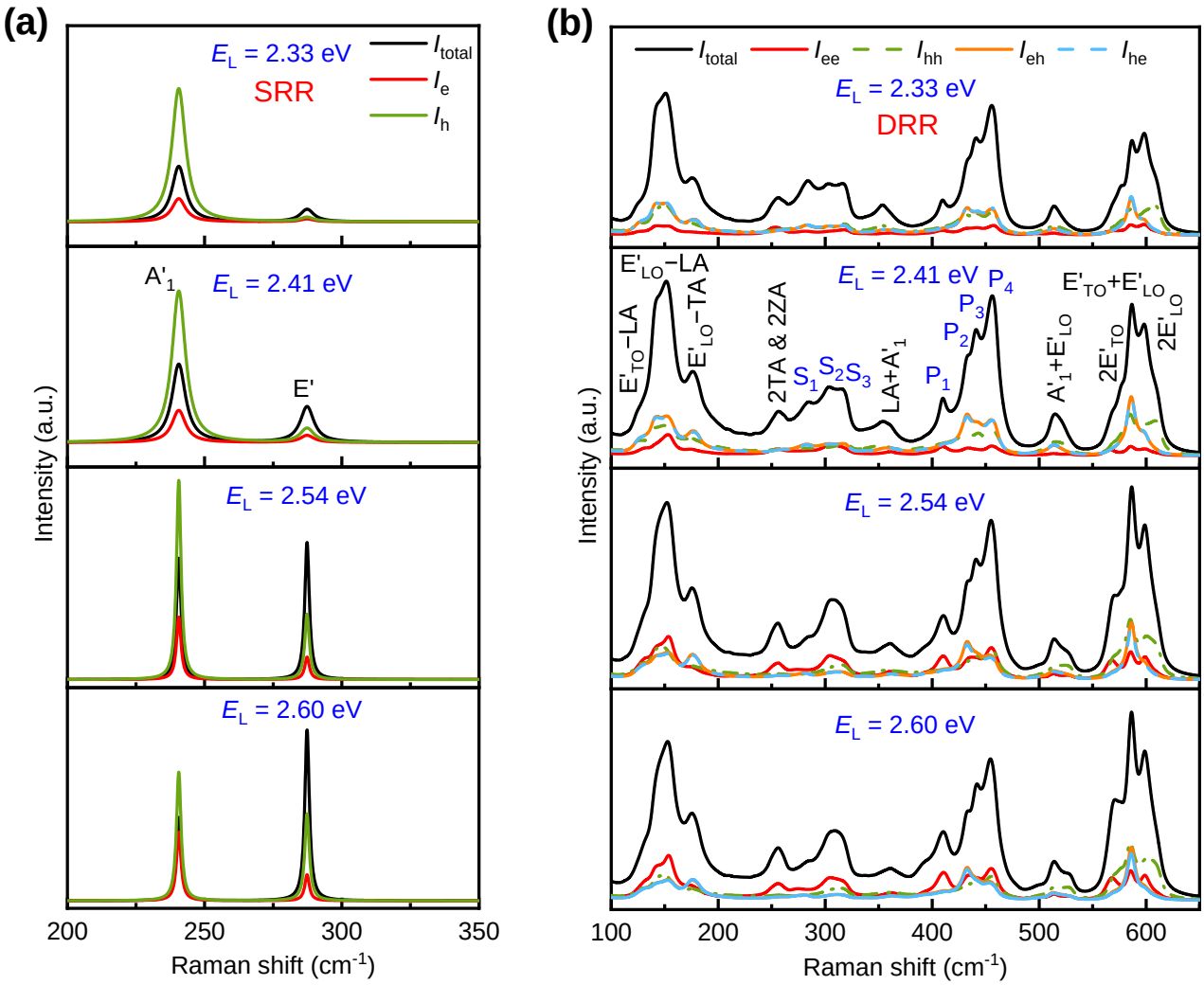


FIG. S7. Decomposition of total Raman spectra into different Raman scattering process pathways: (a) single resonance Raman (SRR) scattering, including *e* and *h* sub-processes, and (b) double resonance Raman (DRR) scattering, including *ee*, *hh*, *eh* and *he* sub-processes. (a) and (b) do not share the value of vertical axis.

[1] P. Tan, Y. Deng, and Q. Zhao, Temperature-dependent Raman spectra and anomalous Raman phenomenon of highly oriented pyrolytic graphite, Phys. Rev. B **58**, 5435 (1998).

[2] K. Gołasa, M. Grzeszczyk, P. Leszczyński, C. Faugeras, A. A. L. Nicolet, A. Wysmołek, M. Potemski, and A. Babiński, Multiphonon resonant Raman scattering in $MoS_2$, Appl. Phys. Lett. **104**, 092106 (2014).